A design optimization methodology for Li+ batteries

Stephanie Golmon [a,b], Kurt Maute [a,b,*], Martin L. Dunn [a,c]

[a] Department of Aerospace Engineering Sciences, University of Colorado, Boulder, CO 80309, USA
[b] Department of Aerospace Engineering Sciences, University of Colorado, Boulder, CO 80309, USA
[c] Department of Mechanical Engineering, University of Colorado, Boulder, CO 80309, USA

HIGHLIGHTS

- A formal design optimization methodology for functionally graded electrodes of Li+ batteries is developed.
- A multi-scale finite element model for predicting the power-storage characteristics of a full battery cell is presented.
- A multi-objective formulation is introduced to optimize the useable capacity over a range of discharge currents.
- The influence of spatially varying porosity and sizes of active particles on optimized electrodes is analyzed.
- The difference between considering a half-cell versus a full cell in the optimization process is shown.

ARTICLE INFO

ABSTRACT

Design optimization for functionally graded battery electrodes is shown to improve the usable energy capacity of Li batteries predicted by computational simulations and numerically optimizing the electrode porosities and particle radii. A multi-scale battery model which accounts for nonlinear transient transport processes, electrochemical reactions, and mechanical deformations is used to predict the usable energy storage capacity of the battery over a range of discharge rates. A multi-objective formulation of the design problem is introduced to maximize the usable capacity over a range of discharge rates while limiting the mechanical stresses. The optimization problem is solved via a gradient based optimization. A $LiMn_2O_4$ cathode is simulated with a $PEO-LiCF_3SO_3$ electrolyte and both a Li Foil (half cell) and LiC_6 anode. Studies were performed on both half and full cell configurations resulting in distinctly different optimal electrode designs. The numerical results show that the highest rate discharge drives the simulations and the optimal designs are dominated by Li+ transport rates. The results also suggest that spatially varying electrode porosities and active particle sizes provides an efficient approach to improve the power-to-energy density of Li+ batteries. For the half cell configuration, the optimal design improves the discharge capacity by 29% while for the full cell the discharge capacity was improved 61% relative to an initial design with a uniform electrode structure. Most of the improvement in capacity was due to the spatially varying porosity, with up to 5% of the gains attributed to the particle radii design variables.

© 2013 Elsevier B.V. All rights reserved.

1. Introduction

Further advances in the energy density, rate capability, and cycling efficiency of batteries are needed in order to meet growing energy storage demands. The essential characteristics of a battery are typically represented via (1) Ragone plots showing the tradeoff between energy storage capacity and power (or rate) capability of the battery and (2) cycling efficiency values which measure the loss in energy storage capacity as a function of cycle number. In this paper, we focus on the trade-off between power and energy densities with consideration of mechanical stress levels that could lead to degradation over time. We do not explicitly model degradation phenomena such as loss of lithium due to side reactions and SEI layer formation and mechanical fracture [1]; instead we consider approximately mechanical degradation by introducing a stress limit in the electrode particles.

In general the energy storage capacity, or usable capacity decreases, with increasing rate or power demand as seen in Fig. 1. Here, we define the usable capacity as the amount of energy that can be extracted from the battery during discharge. In this study, we will show that the decrease in usable capacity at higher discharge rates can be mitigated by optimally designing the internal electrode structure based on the range of rates required from

---

* Corresponding author. Department of Aerospace Engineering Sciences, University of Colorado, Boulder, CO 80309, USA.
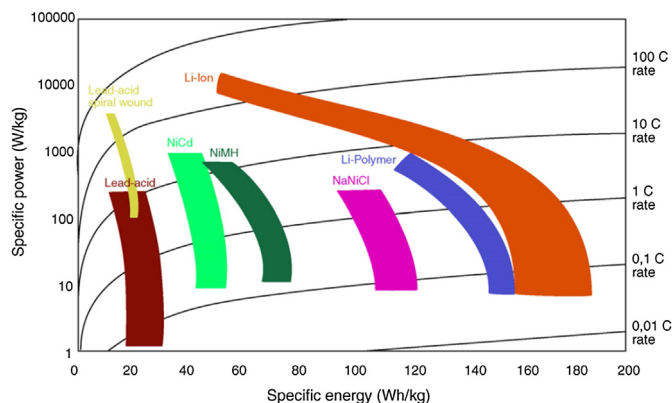E-mail address: maute@colorado.edu (K. Maute).

Fig. 1. Ragone plot comparing battery technologies [34].

the battery for a given application. We focus the study on lithium batteries which are among the most promising battery chemistries due to their high energy densities and operating voltages. Design variables for the battery electrode include the local porosity and particle radii distributions in the electrodes. Additional design variables such as the electrode thickness and material properties can be incorporated into this approach. We formulate this design problem via a multi-objective formulation, maximizing the usable capacity at various discharge rates while constraining the stress levels in the electrode particle to be below a specified maximum value. The optimization problem is solved via a gradient-based algorithm which allows for a large number of both design constraints and optimization variables. The battery simulation uses a transient, non-linear, multi-scale framework to simulate the discharge of the battery at prescribed rates. The sensitivities of the objective and constraints to the design variables are calculated via a multi-scale adjoint approach which is more accurate and efficient than computation of the sensitivities via finite differencing [2]. Adjoint sensitivity analysis combined with a gradient-based optimization algorithm drives the problem to the optimal electrode structure.

This paper is aimed at advancing the state-of-the-art in model-based optimization for Li batteries. Previous optimization studies for Li battery performance have focused on pack-level thermal [3–5] and power management [6] strategies. Design studies focusing on the cell level have been severely limited in number of design variables due to the complexity and computational cost of most battery models [7–10]. This brief literature review does not include design studies based on experimental investigations and parameter sweeps. Here, we are not limited in number of design variables due to our use of multi-scale adjoint sensitivity analysis developed by Golmon et al. [2]. Our approach is flexible, allowing for different types of objectives, constraints, and types of design variables without compromising the accuracy of the overall model. Possible optimization variables include but are not limited to: the electrode porosity and particle size, discharge rate(s), electrode thickness, and material properties. In this study, we focus on improving the discharge performance of the battery through functionally graded electrodes by optimizing the porosity and radii distribution in both electrodes over a range of discharge rates. We consider the effects of Li^+ transport in the electrolyte, Li transport in the electrode particles, local electrode surface kinetics, diffusion-induced stresses in the electrode particles and resulting aggregate swelling of the electrode. Solid electrolyte interphase (SEI) layer growth, chemical side reactions, thermal effects, and degradation effects from cycling and aging are not included. The optimization approach used here could be extended to more sophisticated models such as that of Kim et al. [11].

2. Multi-scale battery model

A typical Li battery is shown in Fig. 2 and consists of current collectors, porous electrodes and a separator region. The porous electrode includes active insertion compounds, conductive additives, and binders with electrolyte filling the pores. The liquid volume fraction of electrolyte is referred to as the porosity, ε, and in a typical battery is 30% [12]. When the battery is discharged, Li in the anode oxidizes. Electrons flow through the external circuit to the cathode and lithium ions, Li^+ are carried through the electrolyte via diffusion and migration to the cathode, where they are reduced. In modern Li batteries, Li inserts into a host electrode material rather than plating onto metals, and these compounds shrink and swell as a result of the Li insertion and de-insertion. The resulting stresses can exceed the fracture toughness of the active particle and experimental studies have linked mechanical effects with capacity fade [13] and localized degradation of the electrode [14]. Stress-induced surface cracks in electrode particles have been shown to nucleate new SEI layer growth and substantially contribute to the loss of Li, causing capacity fade [1]. These studies demonstrate that it is necessary to consider mechanical effects when optimizing the electrode structure in order to limit mechanical degradation. In this study, we define performance in terms of the trade-off between usable energy and power density during discharge of the battery. To minimize mechanical degradation over the life cycle of the battery, we limit electrode stress levels during discharge.

Here, we use a coupled electrochemical–mechanical multi-scale model to simulate the discharge of Li batteries [15]. This model is an extension of Doyle and Newman's electrochemical battery model [16–20] which describes the transport processes within the electrodes using porous electrode theory [21,20] rather than modeling the detailed geometry of the composite electrode. We have extended this model to include deformations due to external mechanical loads and swelling of electrode particles upon lithiation. This model explicitly considers two length scales: at the macro-scale, transport processes in the electrolyte, electric potentials in both the electrolyte and electrode, and mechanical deformations across the battery cell are described; at the micro-scale, the response of a single electrode particle is modeled; a meso-scale model is used to relate these two scales using volume averaging homogenization methods. The effective macro-scale properties are computed as a function of the micro-scale state variables at each time-step in the transient simulation. Qualitative comparisons of discharge curves generated by the electrochemical portion of this model with experimental studies have shown good agreement [22].

In the following sub-sections, we summarize the governing equations used to describe the battery behavior at the macro-scale, micro-scale and the homogenization approaches used to connect the two scales at the meso-scale.

2.1. Governing equations at macro-scale

At the macro-scale, the Li^+ concentration in the electrolyte, c_l, electric potentials in the solid, ϕ_1, and liquid, ϕ_2, phases, and displacements, $\mathbf{u}$, are modeled.
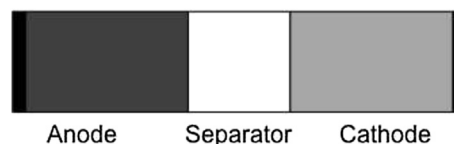

Fig. 2. Battery cell.

Lithium ions are transported through the electrolyte via diffusion and migration:

$$\varepsilon \frac{\partial c_l}{\partial t} + \nabla \cdot \mathbf{N} + \frac{1}{F}\frac{\partial t_+^0}{\partial c_l}\mathbf{i}_2 \cdot \nabla c_l - \left(1 - t_+^0\right)j_{\text{eff}} = 0, \tag{1}$$

where $\mathbf{N}$ is the diffusive flux, t_+^0 is the Li$^+$ transference number, F is the Faraday constant, and j_{eff} is a source term which accounts for the volume average flux of Li$^+$ from the electrolyte into the electrode particles.

Within the solid (electrode), the electric potential is governed by Ohm's law:

$$\nabla \cdot \mathbf{i}_1 + Fj_{\text{eff}} = 0. \tag{2}$$

Similarly, the electric potential in the electrolyte is governed by a modified Ohm's law that accounts for the dependence of the current in the electrolyte, $\mathbf{i}_2$, on the concentration of Li$^+$ in the electrolyte, c_l.

$$\nabla \cdot \mathbf{i}_2 - Fj_{\text{eff}} = 0. \tag{3}$$

The macro-scale mechanical response is assumed to be linear-elastic with a volume-averaged eigenstrain model to account for swelling of the micro-scale electrode particles:

$$\nabla \cdot \boldsymbol{\sigma} + \mathbf{b} = 0, \tag{4}$$

where $\boldsymbol{\sigma}$ and $\mathbf{b}$ are the macro-scale stress tensor and body force. Here, the body force is assumed to be zero.

The diffusive flux, electric currents, stress and strains are described by the following constitutive equations:

$$\mathbf{N} = -D_{\text{eff}}\nabla c_l, \tag{5}$$

$$\mathbf{i}_1 = -\lambda\nabla\phi_1, \tag{6}$$

$$\mathbf{i}_2 = -\kappa_{\text{eff}}\left[\nabla\phi_2 - \frac{RT}{F}\left(1 - t_+^0\right)\nabla\ln(c_l)\right], \tag{7}$$

$$\boldsymbol{\sigma} = \mathbf{C} : (\mathbf{e} - \mathbf{e}_{\text{ch}}), \mathbf{e} = \frac{1}{2}\left(\nabla\mathbf{u} + \nabla\mathbf{u}^T\right), \tag{8}$$

where D_{eff} is the effective diffusion coefficient of Li$^+$ in the electrolyte, λ is the conductivity of the electrode particles, κ_{eff} is the effective ionic conductivity of the electrolyte, $\mathbf{C}_{\text{eff}}$ is the homogenized elasticity tensor, and $\mathbf{e}_{\text{ch}}$ is the volume-averaged chemically induced eigenstrain due to the aggregate swelling of the electrode particles. More complex mechanical models to capture nonlinear stress–strain relationships, finite strains, and irreversible deformations could be included in this framework.

For a galvanostatic discharge of the battery, boundary conditions are applied as follows: at the anode-current collector boundary, Γ_{AC}, and cathode-current collector boundary, Γ_{CC}, all the current is carried by the electrode particles. The boundary conditions are given in columns two and three of Table 1.

To simplify the computational burden of these simulations, we also model a Li half cell, in which a porous cathode is discharged against a Li foil anode; the anode is modeled through boundary conditions at the anode-separator interface. At the anode-separator boundary, Γ_{AS}, Li$^+$ enters the electrolyte based on the rate of discharge, I, and all current is carried by the electrolyte. At the cathode-current collector the conditions remain the same. These boundary conditions are shown in columns three and four of Table 1.

Table 1
Boundary conditions for macro-scale battery model.

	Anode-current collector boundary, Γ_{AC}	Cathode-current collector boundary, Γ_{CC}	Anode-separator boundary, Γ_{AS}
Li$^+$ flux	$\nabla c_l = 0$	$\nabla c_l = 0$	$\mathbf{N} = \frac{I(1-t_+^0)}{F}$
Current in solid particles	$\mathbf{i}_1 = I$	$\mathbf{i}_1 = I$	$\mathbf{i}_1 = 0$
Current in electrolyte	$\mathbf{i}_2 = 0$	$\mathbf{i}_2 = 0$	$\mathbf{i}_2 = I$
Displacements	$\mathbf{u} = 0$	$\mathbf{u} = 0$	$\mathbf{u} = 0$

2.2. Governing equations at micro-scale

At the micro-scale, the response of a single electrode particle embedded in the host electrode is modeled. We assume that the macro-scale Li$^+$ concentration, electric potentials, and displacement fields are spatially constant in the electrolyte immediately surrounding the particle. Assuming the micro-scale particles are spherical results in uniform boundary conditions and allows for simplification of the micro-scale model to one dimension using spherical coordinates. The micro-scale model is based on the coupled diffusion-stress model developed by Zhang et al. [23], and extended to include Butler–Volmer surface kinetics and surface pressures.

The concentration, c_s, and deformation, u_r, fields within the particle are described by diffusion and linear static mechanical models:

$$\frac{\partial c_s}{\partial t} + \left(\frac{\partial}{\partial r} + \frac{2}{r}\right)\mathbf{J} = 0, \tag{9}$$

$$\frac{d\sigma_R}{dr} + \frac{2}{r}(\sigma_R - \sigma_T) = 0, \tag{10}$$

with the following constitutive equations:

$$\mathbf{J} = -D_s\left(\nabla_r c_s - \frac{\Omega c_s}{RT}\nabla_r \sigma_h\right), \tag{11}$$

$$\sigma_R = \frac{E}{(1+\nu)(1-2\nu)}\left((1-\nu)\nabla u_r + 2\nu\frac{u}{r} - \frac{\Omega}{3}c_s(1+\nu)\right), \tag{12}$$

$$\sigma_T = \frac{E}{(1+\nu)(1-2\nu)}\left(\frac{u}{r} + \nu\nabla u_r - \frac{\Omega}{3}c_s(1+\nu)\right), \tag{13}$$

where D_s is the diffusion coefficient of Li in the particle; R is the universal gas constant; T is the temperature; σ_R, σ_T, and σ_h are the radial, tangential, and hydrostatic stresses; E and ν are the Young's modulus and Poisson's ratio of the electrode material. The Li partial molar volume, Ω, accounts for the swelling of the particle upon lithiation and the stress–diffusion coupling increases with Ω. The hydrostatic stress is defined as:

$$\sigma_h = (\sigma_R + 2\sigma_T)/3. \tag{14}$$

At the particle center, $r = 0$, the displacements and Li flux are zero, $u_r = 0, \mathbf{J} = 0$. At the particle surface, $r = R_s$, Li enters the particle and mechanical surface pressure is applied.

$$\mathbf{J} = j_s \text{ at } r = R_s, \tag{15}$$

$$\sigma_R = P_{\text{micro}} \text{ at } r = R_s. \tag{16}$$

The Li pore wall flux at the particle surface, j_s, is described by the Butler–Volmer surface kinetics model which predicts the current/Li flux across the boundary as a function of the electric potentials and concentrations in both phases:

$$j_s = \frac{i_0}{F}\left[c_{s|r=R_s}e^{k_1} - \left(c_{s,\max} - c_{s|r=R_s}\right)e^{k_2}\right], \tag{17}$$

$$
\begin{aligned}
i_0 &= FK_2\left(c_{l,\max} - c_l\right)^{\alpha_C}(c_l)^{\alpha_A}, \\
k_1 &= \frac{\alpha_A F}{RT}\left(\eta - U'\left(c_{s|r=R_s}\right)\right), \\
k_2 &= -\frac{\alpha_C F}{RT}\left(\eta - U'\left(c_{s|r=R_s}\right)\right), \\
\eta &= \phi_1 - \phi_2,
\end{aligned} \tag{18}
$$

where $c_{s,\max}$ and $c_{l,\max}$ are the maximum Li and Li$^+$ concentrations in the electrode particle and electrolyte; α_A and α_C are the anodic and cathodic transfer coefficients; η is the surface overpotential; and $U'(c_{s|r=R_s})$ is the open circuit potential as a function of Li concentration.

The surface pressure, P_{micro}, has contributions due to the inclusion of the particle in the swelling aggregate, P_h, and from surface stress, P_{SS}, which can be written for spherical particles as [24]:

$$P_{\text{micro}} = P_h + P_{SS}, \tag{19}$$

$$P_{SS} = -2\frac{\tau_0 + K^s \varepsilon_T|_{r=R_s}}{R_s}, \tag{20}$$

where τ_0 is the deformation-independent surface tension, K^s is the surface modulus, and ε_T is the tangential strain, which in spherical coordinates is defined as: $\varepsilon_T = u_r/r$. The model presented here does not include more complex phenomena such as non-Fickian diffusion, the effects of chemical potential on stress, finite strains, and plastic deformations [25–27].

2.3. Governing equations at meso-scale

The influence of the micro-scale particles on the macro-scale is seen through the effective pore wall flux, j_{eff}, and chemical chemically induced eigenstrain $\mathbf{e}_{\text{ch}}$. Similarly, the microscopic pore wall flux, j_s, and surface pressure, P_h depend on both macro- and micro-scale state variables. Aggregate theory [28] and Bruggeman relations [16,20] are used to relate the scales. The effective pore wall flux is related to the micro-scale pore wall flux through:

$$j_{\text{eff}} = \frac{3(1-\varepsilon)}{R_s}j_s. \tag{21}$$

The porosity of the electrode influences the effective properties D_{eff} and κ_{eff} which are found via Bruggeman relations based on the diffusion coefficient D_l and electrolyte conductivity, κ_∞ in the bulk electrolyte:

$$
\begin{aligned}
D_{\text{eff}} &= \varepsilon D_l, \\
\kappa_{\text{eff}} &= \varepsilon^{3/2}\kappa_\infty.
\end{aligned} \tag{22}
$$

The micro-scale surface pressure and macro-scale chemically induced eigenstrain depend on macro- and micro-scale strains through the Mori-Tanaka model [28–30]. Here, we assume there is no chemically induced strain in the electrolyte.

$$P_h = \left(\mathbf{b}_s + \mathbf{B}_s\mathbf{C}_{\text{eff}}(\mathbf{e} - \mathbf{e}_{\text{ch}})\right)\hat{\mathbf{n}}, \tag{23}$$

$$\mathbf{e}_{\text{ch}} = (1-\varepsilon)\mathbf{e}_V + (1-\varepsilon)\left(\mathbf{C}_s^{-1} - \mathbf{C}_l^{-1}\right)\mathbf{b}_s, \tag{24}$$

where $\mathbf{C}_l$ and $\mathbf{C}_s$ are the isotropic constitutive tensors of the electrolyte and active particles and $\mathbf{C}_{\text{eff}}$ is the effective material tensor of the composite electrode. The matrices $\mathbf{B}_s$ and $\mathbf{b}_s$ are

homogenization operators; for details, the reader is referred to references [15] and [2].

The micro-scale volumetric strain, $\mathbf{e}_V$ is found via:

$$\mathbf{e}_V = \frac{1}{3}\left(\frac{\left(R_s + u_{r|r=R_s}\right)^3}{R_s^3} - 1\right). \tag{25}$$

2.4. Ragone plot simulation

The set of equations presented in Sections 2.1–2.3 is used to predict the Ragone curve for the battery by simulating the discharge of the battery over a range of rates. We discharge the battery using a Li$_x$C$_6$ anode, PEO–LiCF$_3$SO$_3$ electrolyte, Li$_y$Mn$_2$O$_4$ cathode system where $0 \leq x \leq 1$ and $0 \leq y \leq 1$. Material properties are given in Tables 2–4. For the simulations in this paper, the separator is 50 μm thick and the cathode is 100 μm thick. This yields a theoretical capacity of the battery of 34.8 Ah m^{-2}. The theoretical capacity for a given design is the minimum of the anode and cathode capacities upon discharge. For the cathode, the theoretical capacity is the amount of cathode active material multiplied by the amount of Li that can be intercalated into the cathode particles:

$$\int_{x=\delta_{SC}}^{x=\delta_{CC}} (1-\varepsilon)\mathrm{d}x\left(c_{s,\max} - c_{s,0}\right)*F. \tag{26}$$

Similarly the capacity of the anode is the amount of anode active material multiplied by the amount of Li present in the anode at the start of the discharge:

$$\int_{x=\delta_{AC}}^{x=\delta_{AS}} (1-\varepsilon)\mathrm{d}x * c_{s,0} * F. \tag{27}$$

The thickness of the anode of 142 μm was chosen so that both electrodes would have the same theoretical capacity. The battery is discharged at a constant rate, I, until the potential difference between the electrodes $(\phi_1|_{x=\Gamma_{CC}} - \phi_1|_{x=\Gamma_{AC}})$ reaches the cutoff potential, $\hat{\phi}_1$ of 2.7 V; this cutoff potential was selected due to its position on the discharge curves − as below 2.7 V, the battery potential quickly drops to zero with a negligible increase in capacity.

At both scales, the governing equations are discretized spatially using finite elements and in time using an implicit Euler backwards scheme. An adaptive time stepping algorithm is used that varies the time step size based on the rate of change of the potential difference across the electrodes of the battery. Spatially, we discretize the system using 20 elements in the separator region, 80 elements in each electrode region, and 20 elements in each micro-scale problem. Studies were performed to ensure mesh and time

Table 2
Anode material parameters, Li$_x$C$_6$, $0 \leq x \leq 1$.

Symbol	Value	Units	Description
$c_{s,\max}$	26,400	mol m^{-3}	Maximum Li concentration in cathode
$c_{s,0}$	13,070	mol m^{-3}	Initial Li concentration in cathode
σ_s	100	S m^{-1}	Conductivity in cathode
D_s	5e-13	m^2 s^{-1}	Diffusivity of Li in cathode
E_s	15	GPa	Young's modulus
ν_s	0.3	−	Poisson's ratio
Ω	4.221e-6	m^3 mol^{-1}	Partial molar volume
k_2	1e-10	m^4 mol^{-1} s^{-1}	Butler–Volmer reaction rate constant

Table 3
PEO–LiCF$_3$SO$_3$ electrolyte material parameters.

Symbol	Value	Units	Description
$c_{l,max}$	3920	mol m^{-3}	Maximum Li$^+$ concentration in electrolyte
$c_{l,0}$	2070	mol m^{-3}	Initial Li$^+$ concentration in electrolyte
κ_∞	6.5e-3	S m^{-1}	Conductivity in electrolyte
D_l	7.5e-12	m^2 s^{-1}	Diffusivity of Li in electrolyte
E_l	0.69	MPa	Young's modulus
ν_l	0.4	–	Poisson's ratio

convergence. Two-point Gauss integration is used at the macro-scale which results in 320 micro-scale problems. In total, there are 564 macro-scale state variables, and 33,280 micro-scale state variables.

Fig. 3 is a Ragone plot of the rate versus usable capacity tradeoff seen when the battery is discharged at 14 rates ranging from 0.01 A m^{-2} to 25 A m^{-2}; these results use a uniform porosity of $\varepsilon = 0.3$ and particle radii of 5 μm in both electrodes. At low discharge rates, the battery utilizes up to 99% of the theoretical capacity of the battery. However as the discharge rate increases, there is a significant drop in the usable capacity of the battery. Ideally, the usable capacity of the battery would not decrease with increasing discharge rate.

We compare the discharge of the battery using a carbon anode to a Li foil anode. The theoretical capacity of the battery is the same, however the Li foil provides an effectively unlimited source of Li$^+$ at the anode-separator boundary, Γ_{AS}. As seen in Fig. 3, this shifts the Ragone line to the right, i.e. higher capacities for higher rates. Nevertheless, the decrease in usable capacity for high rates is still seen. The advantage of analyzing the capacity of the half-cell of the cathode cycled vs. a Li foil anode is in the decrease in computational cost as the anode does not need to be discretized. For the computational model used in this study, the number of macro-scale state variables decreases to 404 and the number of micro-scale state variables is halved from 33,280 to 16,640.

When discharging the half-cell, the cutoff potential is set at 3.2 V. The higher cutoff potential as compared to the carbon anode simulations is due to the constant anode potential (versus increasing potential) during discharge for the half-cell simulations. For both types of studies, the cutoff potentials were selected based on reaching the regime in which the overall battery potential quickly drops to zero. Qualitatively, the Ragone plots predicted by this model are in good agreement with experimental results for Li batteries [17].

3. Design optimization

In order to improve the high rate usable capacity of the battery, we optimize the electrode structure when the battery is discharged

Table 4
Cathode material parameters, Li$_y$Mn$_2$O$_4$, $0 \le y \le 1$.

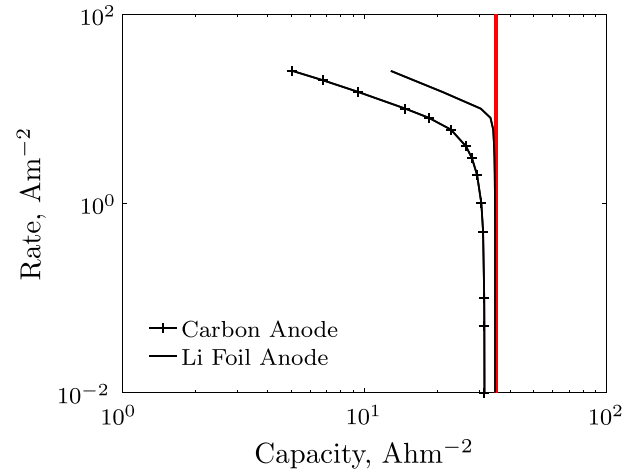| Symbol	Value	Units	Description
$c_{s,max}$	22,900	mol m^{-3}	Maximum Li concentration in cathode
$c_{s,0}$	4351	mol m^{-3}	Initial Li concentration in cathode
σ_s	3.8	S m^{-1}	Conductivity in cathode
D_s	7.08e-15	m^2 s^{-1}	Diffusivity of Li in cathode
E_s	10	GPa	Young's modulus
ν_s	0.3	–	Poisson's ratio
Ω	3.497e-6	m^3 mol^{-1}	Partial molar volume
k_2	1e-10	m^4 mol^{-1} s^{-1}	Butler–Volmer reaction rate constant
τ_0	−0.606	J m^{-3}	Surface tension (Si value)
K^s	10.65	N m^{-1}	Surface modulus (Si value)

Fig. 3. Ragone Plot for full battery simulation with $\varepsilon = 0.3$ and $R_s = 5$ μm, for both types of anodes, the vertical line is the theoretical capacity.

over a range of discharge rates, $I_j, j = 1{:}N_j$, where N_j is the number of rates simulated. Previous studies have shown an influence of the porosity and micro-scale particle radii on the discharge behavior of the battery [15,31,2]. Therefore we consider the local porosities and electrode particle radii in both electrodes as design variables. For a given layout of the electrodes, we simulate the discharge of the battery over the specified range to the cutoff potential and maximize the minimum capacity for the range of discharge rates considered. This max-min multi-objective optimization problem is solved via a bound formulation [32]. To this end, we introduce an auxiliary variable, β:

$$\beta = \min(I_j \hat{t}_j), \tag{28}$$

where $\hat{t}_j$ is the time the battery reaches the cutoff potential when discharged at rate I_j. The objective is to maximize β by manipulating the design variables, **s**. Constraints are placed on the difference, $\beta - I_j \hat{t}_j$, in order to ensure that β is the minimum value. This results in the following problem formulation:

$$\max_{\mathbf{s}} \beta(\mathbf{s})$$
$$s.t. G_j = \beta - I_j \hat{t}_j \le 0 \quad \forall j = 1, ..., N_j. \tag{29}$$

The design variables of the particle radii are limited to be between 1 nm and 10 μm and the porosities are limited to between 0.05 and 0.95 to ensure that both electrode and electrolyte phases are present throughout the electrode. In addition, we place constraints on the maximum stress level in the micro-scale electrode particles during discharge:

$$G_\sigma = \max_t \max_r \max_i \sigma_{T,j,t,r,t} - \sigma_{max} \le 0,$$
$$\forall j = 1{:}N_j, \ t = 1{:}N_{t,j}, \ i = 1{:}N_m, \ r = 1{:}N_r, \tag{30}$$

where r is the node id of the particle finite element model, i the individual micro-scale particle, and t the time step. $N_{t,j}$ is the number of time-steps needed when discharged at rate I_j, N_m is the number of micro-scale particles, and N_r is the number of nodes in the particle model. In this paper, we set σ_{max} to 50 MPa. This stress level was chosen on the basis of stress levels seen in the constant porosity solutions of Ref. [2]. To reduce the number of stress constraints, we approximate the maximum particle stress in an

Table 5
GCMMA parameters.

Parameter	Value
Step size, Δ_s	0.01–0.2
Initial adaptation of asymptotes	0.5
Adaptation of asymptotes	0.7
Maximum number of sub-cycles	1
Relative change in optimization variables	$\Delta_s = 10^{-8}$

individual particle, i, at discharge rate I_j using the Kreisselmeier–Steinhauser (KS) function with $\omega = 3$:

$$\tilde{\sigma}_{T,j,i} = \frac{1}{\omega} \ln \sum_t \sum_r \exp\left(\omega \sigma_{T,j,t,r,i}\right) \quad t = 1 : N_{t,j}, r = 0 : R_s. \tag{31}$$

The accuracy of this approximation has been monitored in the numerical examples to ensure the approximation is accurate to within 0.1% at 50 MPa.

The design optimization problems are solved using the Globally-Convergent Method of Moving Asymptotes (GCMMA) of Svanberg [33]. The GCMMA constructs a sequence of convex separable sub-problems that are solved by a primal-dual method, and is guaranteed to converge to a Karush–Kuhn–Tucker (KKT) optimal point. This algorithm is specifically suited for problems with large numbers of design variables and few inequality constraints as it is the case in the current study. The GCMMA is considered converged if the constraints are satisfied and the relative change in design variables, Δ_s is sufficiently small:

$$\frac{||\mathbf{s}^{m-1} - \mathbf{s}^m||}{||\mathbf{s}^{m-1}||} \leq \Delta_s, \tag{32}$$

where m is the iteration number of the optimization process. Parameters used by the GCMMA are given in Table 5; for a detailed explanation of these parameters, the reader is referred to Ref. [33].

GCMMA requires the derivatives of G_j and G_σ, with respect to the design variables. The derivatives of the objective, β, with respect to the design variables are zero, while the derivatives of the constraints, G_j and G_σ, are nonzero due to the dependence of the simulation time, $\hat{t}_j$, and model behavior on the design variables. Due to the potentially high number of design variables and computational cost of the model, the sensitivities are found using an adjoint approach. The main advantage of this approach is that the numerical costs of computing the design sensitivities are nearly independent of the number of design variables. For the problem of interest, the adjoint sensitivity equations only need to be solved N_G times in each step of the optimization procedure, where N_G is the number of constraints. This involves integrating backward in time the linearized multi-scale model described in Section 2. Details on the formulation, numerical procedure, and computational efficiency of performing adjoint sensitivity analysis for the multi-scale framework are provided in Golmon et al. [2].

4. Design optimization examples

4.1. Optimization of cathode discharged against Li foil anode

We solve the above design optimization problem (29) for a range of discharge rates, $I_j = [0.01:20]$ A m^{-2}, first with a Li foil anode. The cathode is initialized with uniform porosity of 0.3 and particle radii of 5 μm, consistent with the nominal design in previous studies [15]. Fig. 4(a) shows the effect of optimizing the electrode design on the Ragone plot, and Fig. 4(b) and (c) plots the
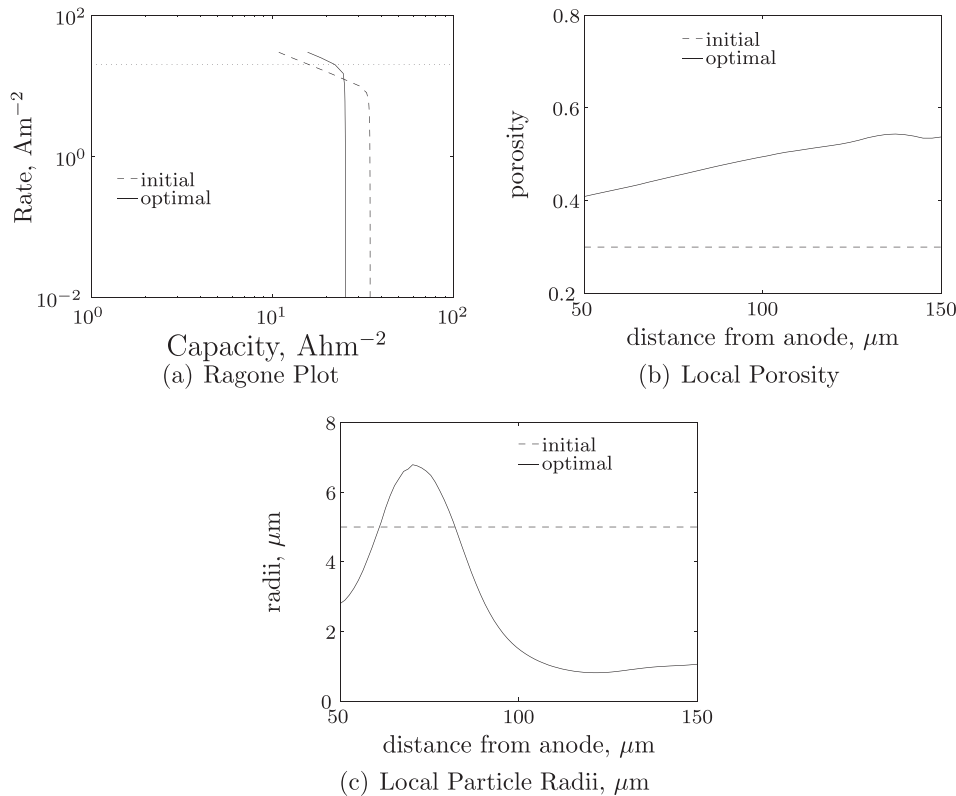

(a) Ragone Plot

(b) Local Porosity

(c) Local Particle Radii, μm

Fig. 4. Ragone plot, porosity and particle radii distributions of initial and optimal designs for design optimization problem with $I_j = [0.01:20]$ A m^{-2}.

initial and optimal porosity and particle radii distributions. A 39% improvement in capacity is obtained at 20 A m^{-2}, however at low rates, there is a 27% decrease in capacity. The theoretical capacity of the battery decreases from 34.80 Ah m^{-2} to 29.8 Ah m^{-2} due to the increased porosity of the electrode. The optimal configuration achieves 75% of the theoretical capacity at 20 A m^{-2} and up to 86% of the theoretical capacity at lower discharge rates. The optimization problem is dominated by the performance at the 20 A m^{-2} discharge rate which has the lowest capacity and highest electrode particle stress levels throughout the optimization process. This would allow for a reduction of the optimization problem to a simple single-objective problem, maximizing the capacity at a discharge rate of 20 A m^{-2}.

The influence of the electrode design on the behavior of the battery is seen in Figs. 5 and 6 which show the Li$^+$ concentration in the electrolyte, the normalized Li concentration in the electrode

particles, and the stress levels in the electrode particle as a function of time and position within the battery for initial and optimal configurations for 10 A m^{-2} and 20 A m^{-2} discharge rates.

Two main mechanisms dominate the discharge process: (1) lithiation of the cathode particles at the back of the electrode as seen in Fig. 5(d), and (2) depletion of Li$^+$ in the electrolyte within the cathode as seen in Figs. 5(a), 6(a) and 6(b). Depletion of Li$^+$ in the electrolyte is undesirable as it prohibits full utilization of the active material. Once the electrolyte is depleted, the potential of the battery drops quickly. The optimal design for these rates increases the porosity towards the back of the electrode which allows for increased Li$^+$ transport in the electrolyte and thus a longer time before depletion occurs. The electrode particle size is decreased near the separator-cathode interface primarily to decrease the stress levels in the particles; smaller particles allow for faster diffusion of Li into the particles, decreasing the stress and strain
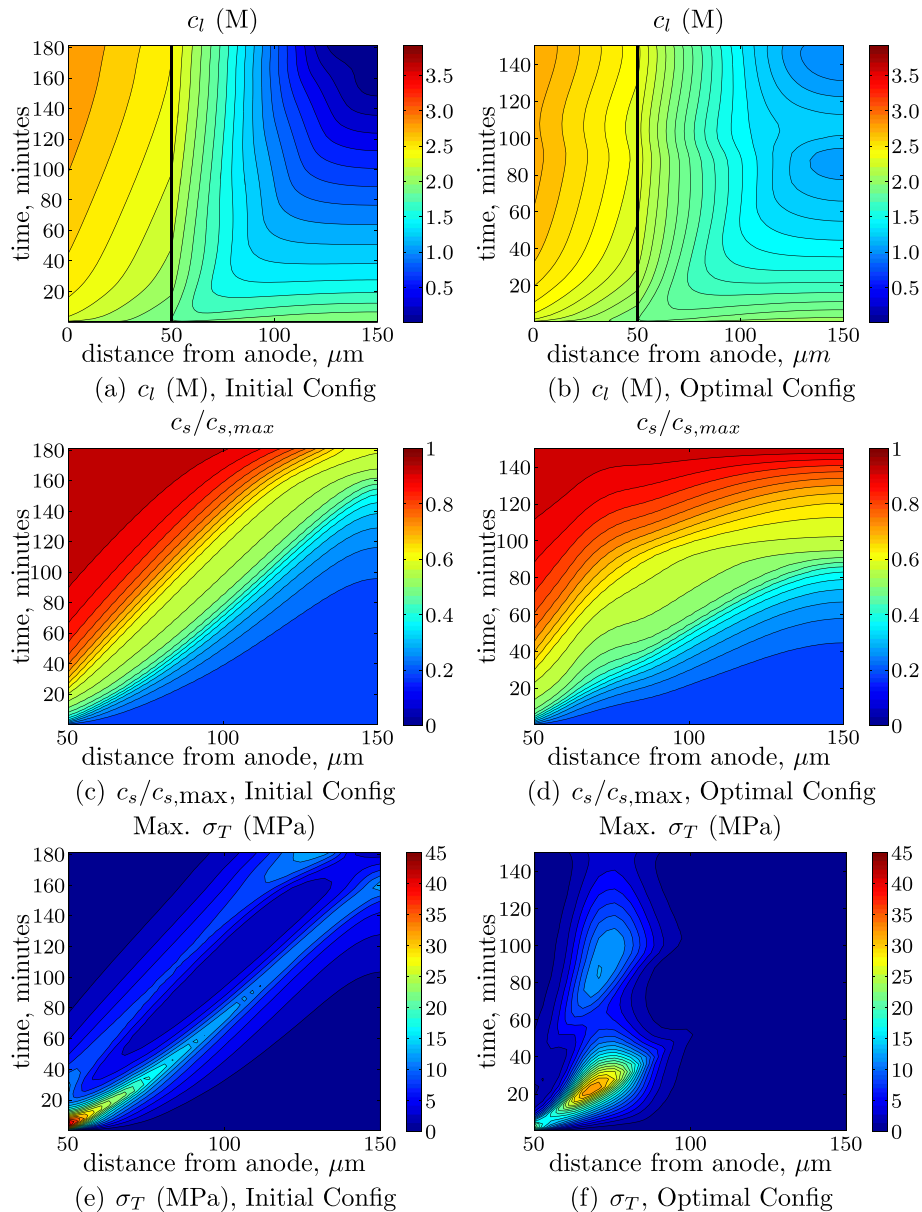

Fig. 5. c_l and c_s concentrations and maximum σ_T as a function of time and position in the battery for initial and optimal configurations when discharged at $I = 10$ A m^{-2} for the optimization problem with $I_j = [0.01{:}20]$ A m^{-2}. The vertical lines in (a) and (b) show the separator-cathode interface.
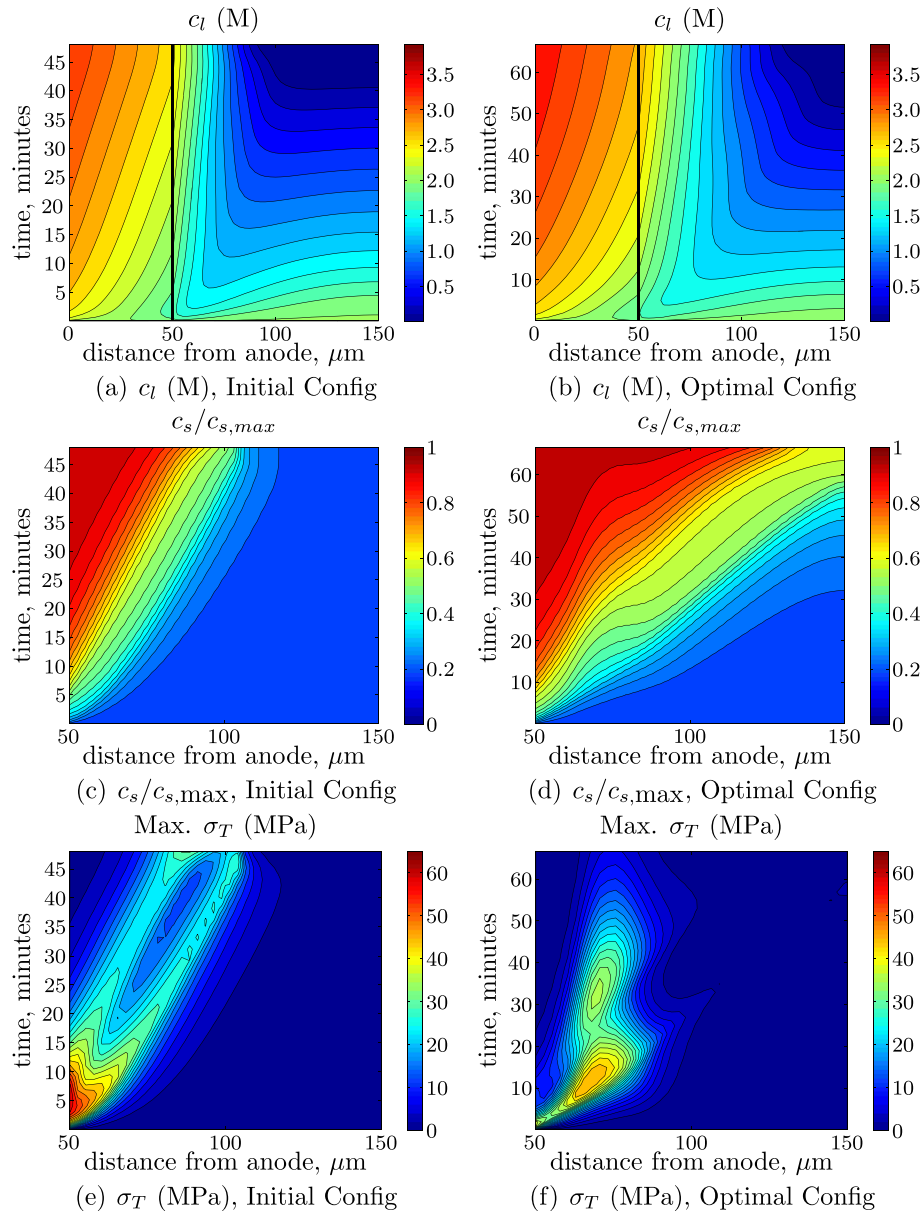
Fig. 6. c_l and c_s concentrations and maximum σ_T values as a function of time and position in the battery for initial and optimal configurations when discharged at $I = 20$ A m^{-2} for the optimization problem with $I_j = [0.01:20]$ A m^{-2}. The vertical lines in (a) and (b) show the separator-cathode interface.

mismatch in the particle. The larger particle sizes slow the rate of Li$^+$ uptake by the particles, which results in enhanced Li$^+$ transport towards the back of the cathode [2]. The optimal porosity distribution is most important in increasing the battery capacity, while adding the radii as design variables allows for a further improvement on the order of 0.5–1 Ah m^{-2}.

For the discharge at 20 A m^{-2} using the initial configuration, only the front half of the cathode is saturated with Li during discharge (Fig. 6(c)) and the cathode particles at the current collector interface only see a negligible increase in Li concentration. The stress constraint level of 50 MPa is exceeded near the separator–cathode interface (Fig. 6(e)).

In contrast, for the optimal configuration, the Li concentration throughout the cathode increases during discharge (Fig. 6(d)) which increases the capacity and percent utilization of the theoretical capacity of the battery. The Li$^+$ concentration at the back of the cathode (Fig. 6(b)) is depleted over a smaller region of the

cathode and occurs later in the discharge. The stress levels in the particles are maintained below 50 MPa (Fig. 6(f)) with the highest stress levels positioned at the largest particle sizes. The "waves" seen in the contour lines for the normalized Li concentration in the cathode particles are due to the interplay between the different Li transport rates in the electrolyte and particles.

If the range of discharge rates is reduced to a range of [0.01:10] A m^{-2} or [0.01:1] A m^{-2}, the capacity of the battery can be increased over what is possible for the [0.01:20] A m^{-2} range. Fig. 7 shows the designs and Ragone plots for all three optimization problems as compared to the initial configuration. The decrease in the rate range to [0.01:10] A m^{-2} results in an optimal design with a theoretical capacity of 33.96 Ah m^{-2} and the [0.01:1] A m^{-2} range optimal design has a theoretical capacity of 45.21 Ah m^{-2}.

At low discharge rates, the low optimal porosities result in higher usable and theoretical capacity of the battery; here the capacity is reaction-rate limited. As the discharge rate is increased,
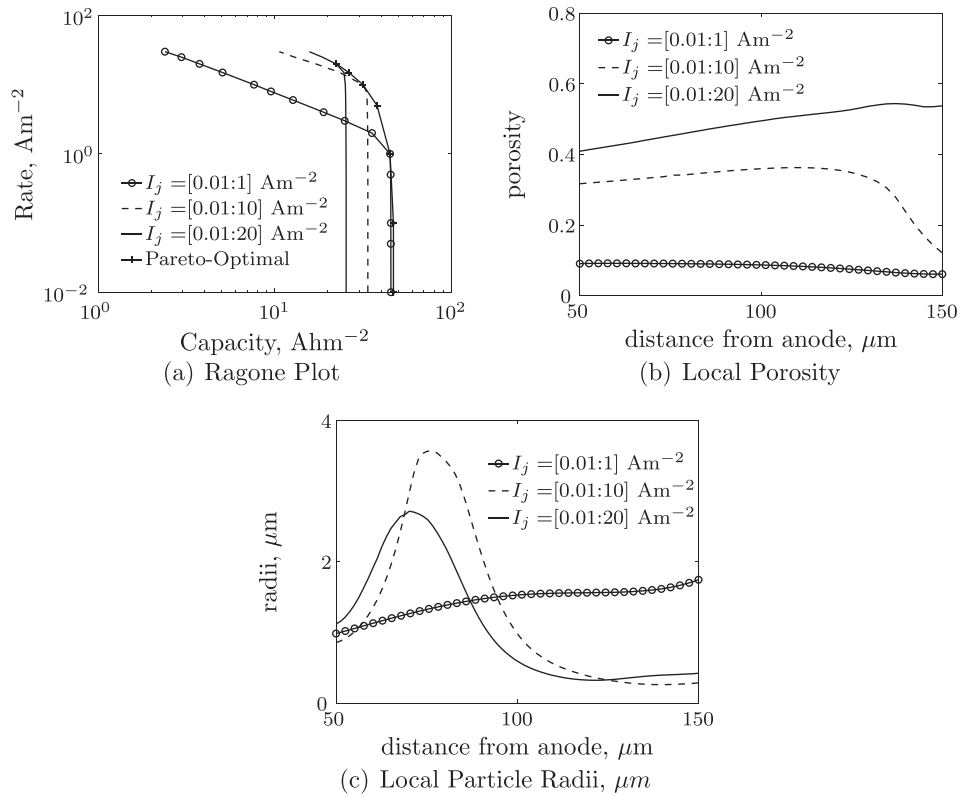
(a) Ragone Plot

(b) Local Porosity

(c) Local Particle Radii, μm

Fig. 7. Ragone plot, porosity and particle radii distributions of initial and optimal designs for all three design optimization problems.

and the transport is limited by diffusion of Li$^+$ in the electrolyte, the porosity is increased which allows for greater Li$^+$ transport. Particle size primarily influences stress levels as large particles are diffusion limited resulting in concentration gradients that cause mismatch strains and stresses due to the stress−diffusion coupling; see Eqns. (12) and (13). With very small particles (<0.5 μm), the stress levels will increase due to the surface stress effect; see Eq. (20). The particle size can also influence the usable battery capacity by effecting the local rate of Li$^+$ uptake throughout the electrode.

A tradeoff is seen between the low and high rate performance of the battery: for the highest rates an increase in usable capacity is shown while the low rates show a decrease in usable capacity. The highest discharge rate dominates the design for each simulation, suggesting that the electrode should be designed based on the highest discharge rate expected during operation. Optimal designs for each discharge rate give upper bounds on what is achievable

with these design variables, giving the Pareto-optimal set of designs (Fig. 7(a)).

As a next step, we replace the Li foil anode with a carbon anode as in Section 2.4, which has the optimal cathode porosity and radii distribution from the Li foil [0.01:20] A m^{-2} discharge rate range. As seen in Fig. 8, the performance improvement is significantly reduced and the overall theoretical capacity of the cell is still reduced by 24%. This result demonstrates that it is necessary to perform the design optimization on the full problem if the carbon anode is to replace the Li foil anode.

4.2. Optimization including carbon anode

The design optimization problem (29) is solved for discharge rates of $I_j = [0.01:1]$ A m^{-2}, $[0.01:10]$ A m^{-2}, and $[0.01:20]$ A m^{-2}, with both anode and cathode porosities and radii as optimization variables. Both electrodes are initialized with uniform porosities of 0.3 and particle radii of 5 μm. For simplicity, the stress constraint (30) is applied only in the cathode region.

Simultaneously optimizing the porosity and particle size distributions in a full battery cell results in greater capacity improvement than using the optimal cathode design with the Li foil anode. As shown in Fig. 9, the resulting optimal design for the [0.01:20] A m^{-2} range improves the capacity of the battery by 61% relative to the initial configuration when discharged at 20 A m^{-2}, while at low discharge rates the capacity is decreased by 42%. Similar levels of improvement are seen at the [0.01:1] A m^{-2} and [0.01:10] A m^{-2} rate ranges. The resulting optimal designs are depicted in Fig. 10. This figure also shows the optimal cathode configuration for the Li foil anode optimization problem for the [0.01:20] A m^{-2} discharge rate range.

The high porosity towards the separator region of the battery in both electrodes is due to the limited amount of Li available in the
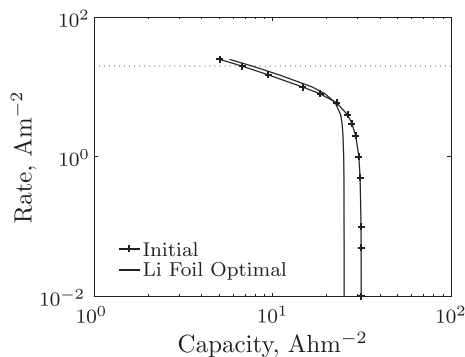

Fig. 8. Ragone plot for the cathode found via optimization of the cathode with a Li foil anode when discharged with a carbon anode.
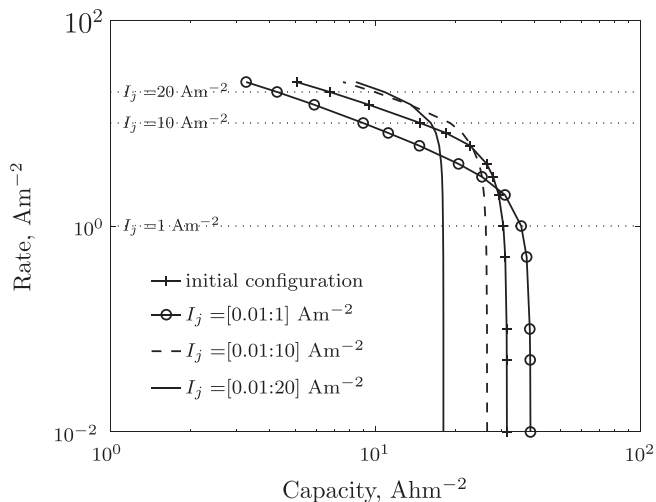
Fig. 9. Ragone plot for initial and optimal configurations for the carbon anode optimization problems.

and electrolyte in the cathode than the anode, resulting in a larger spatial variation of the radii in the cathode.

To further understand the transport limitations of the battery, in Fig. 11 we examine the internal Li^+, normalized Li concentration, and stress fields within the battery for the initial and optimal designs at a 20 A m^{-2} discharge rate. The initial configuration limits the reactions in the electrodes to the region closest to the separator; the slow Li^+ transport limits the amount of the electrodes utilized. The optimal configuration shows reactions occurring throughout both electrodes, although Li^+ depletion is still the limiting factor. In the initial configuration, the stress levels in the cathode exceed the stress constraint level as shown in Fig. 11(e). The stress levels in the optimal configuration were decreased primarily via the increased porosity and the variation in particle radii enhances Li^+ transport through the depth of the cathode.

The study above shows that optimizing both electrodes simultaneously results in greater improvements in usable capacity than optimizing a half cell. Note, that these simulations were performed for a discharge of the battery and result in asymmetric designs between the anode and cathode, optimization of a full charge/discharge cycle could change the optimal configuration.

5. Conclusion

In this paper, a design optimization approach based on a multi-scale battery cell model has been presented and applied to optimizing the electrode design, in order to increase the usable capacity of a battery over a range of discharge rates. Optimal porosity and radii distributions in the battery electrodes were found via a multi-objective design problem with constraints placed on the stress levels in the cathode particles. Studies were performed on both a Li-foil half cell and carbon anode full cell configurations which resulted in different optimal designs. For all studies, the highest rate discharge dominated the performance and the porosity design variables had a greater influence on the usable capacity than the particle radii design variables. Simulations presented showed that the transport of Li^+ in the electrolyte was the dominate process driving the optimal designs resulting in increasing porosities with increasing rates. The particle radii design variables were important in stress-mitigation near the separator-cathode interface and served to further enhance the Li^+ transport due to the effect of particle size on the rate at which Li^+ enters the particles. A tradeoff was observed between low and high rates because the highest rate of discharge drives the optimization problem.

Design optimization of the electrode porosities and particle radii resulted in a 39% increase in capacity for the Li-foil half cell and a 61% increase in capacity for the full cell versus the non-graded design at the 20 A m^{-2} discharge rate. However the optimization results are limited by the level of accuracy of the model which does not include effects such as solid electrolyte interphase (SEI) layer growth, chemical side reactions, and other degradation phenomena. Only a single discharge of the battery was simulated, and optimizing the electrode configuration over a full charge/discharge cycle may result in different optimal electrode structures. Further optimization studies over a full charge/discharge cycle and over multiple cycles, including degradation mechanisms, additional design variables of the electrode thicknesses, and at higher discharge rates are recommended.

Nevertheless, the results presented in this paper suggest that functionally grading the electrode can improve the overall battery performance allowing for greater usable energy density in a battery. Furthermore, this study has demonstrated the utility of computational design optimization as an efficient tool for the development of battery cells. As our optimization approach can incorporate a large number of design variables and can be extended
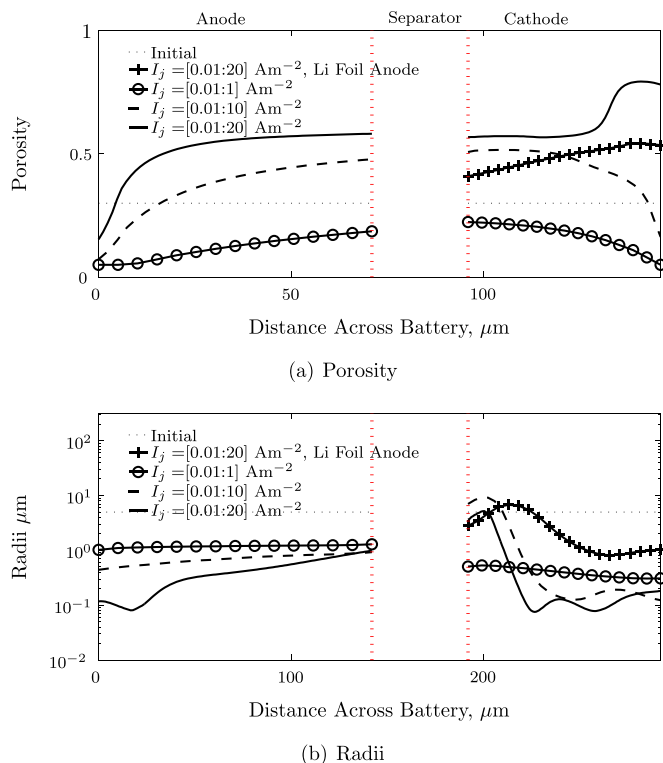
anode as opposed to the effectively unlimited Li source when a Li foil anode is simulated. Increasing the porosity towards the separator region increases the Li^+ transport rates in the electrolyte allowing a higher percentage of the electrodes to be lithiated. At the highest rate, the cathode porosity is further increased at the back of the cathode to allow for increased Li^+ transport in the electrolyte. In the anode, the optimal particle radii distributions result in a small improvement in Li^+ transport in the electrolyte while in the cathode, the stress constraint also influences the distribution. There is a greater difference in diffusion coefficients between the electrode

(a) Porosity

(b) Radii

Fig. 10. Initial and optimal electrode designs for dual electrode optimization. The additional dashed lines in the cathode region are the optimal designs for the Li foil anode optimization problem.
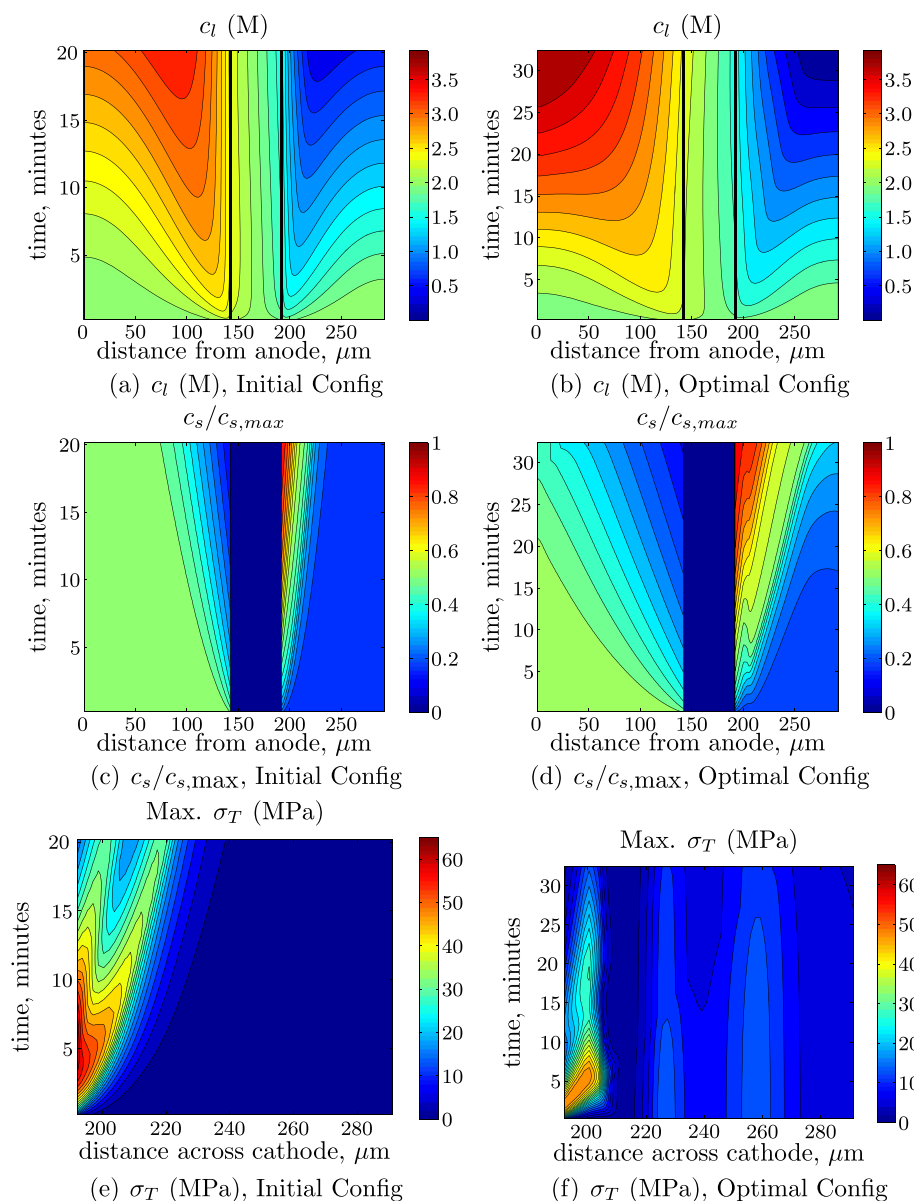
Fig. 11. c_l and c_s concentrations and maximum σ_T as a function of time and position in the battery for initial and optimal configurations when discharged at $I = 20$ A m^{-2} for the full battery optimization problem. The vertical lines show the anode-separator and separator-cathode interface.

onto more complex micro- and macro-scale models, this method could be applied to simulations investigating the overall battery cell design such as those in Ref. [11].

References

[1] R. Deshpande, M. Verbrugge, Y.-T. Cheng, J. Wang, P. Liu, J. Electrochem. Soc. 159 (2012) A1730–A1738.
[2] S. Golmon, K. Maute, M.L. Dunn, Int. J. Numer. Methods Eng. 92 (2012) 475–494.
[3] Y. Chen, J.W. Evans, Electrochim. Acta 39 (1994) 517–526.
[4] L.-J. Yu, M.-J. Qin, P. Zhu, L. Yang, J. Power Sources 179 (2008) 848–853.
[5] A. Jarrett, I.Y Kim, J. Power Sources (2011) 10359–10368.
[6] M.-J. Kim, H. Peng, J. Power Sources 165 (2007) 819–832.
[7] W. Du, A. Gupta, X. Zhang, A.M. Sastry, Int. J. Heat Mass Transfer 53 (2010) 3552–3561.
[8] Y.-H. Chen, C.W. Wang, X. Zhang, A.M. Sastry, J. Power Sources 195 (2010) 2851–2862.
[9] V. Ramadesigan, R.N. Methekar, F. Latinwo, R.D. Braatz, V.R. Subramanian, J. Electrochem. Soc. 157 (2010) A1328–A1334.
[10] S.K. Rahimian, S. Rayman, R.E. White, J. Power Sources 196 (2011) 10297–10304.
[11] G.-H. Kim, K. Smith, K.-J. Lee, S. Santhanagopalan, A. Pesaran, J. Electrochem. Soc. 158 (2011) A955–A969.
[12] M. Winter, R.J. Brodd, Chem. Rev. 104 (2004) 4245–4269.
[13] D. Wang, X. Wu, Z. Wang, L. Chen, J. Power Sources 140 (2005) 125–128.
[14] H. Wang, Y.-I. Jang, B. Huang, D.R. Sadoway, Y.-M. Chiang, J. Electrochem. Soc. 146 (1999) 473–480.
[15] S. Golmon, K. Maute, M.L. Dunn, Comput. Struct. 87 (2009) 1567–1579.
[16] M. Doyle, T.F. Fuller, J. Newman, J. Electrochem. Soc. 140 (1993) 1526–1533.
[17] T.F. Fuller, M. Doyle, J. Newman, J. Electrochem. Soc. 141 (1994a) 1–10.
[18] T.F. Fuller, M. Doyle, J. Newman, J. Electrochem. Soc. 141 (1994b) 982–990.
[19] M. Doyle, J. Newman, Electrochim. Acta 40 (1995) 2191–2196.

[20] M. Doyle, Design and Simulation of Lithium Rechargeable Batteries (Ph.D. thesis), University of California, Berkeley, 1995.

[21] J. Newman, K.E. Thomas, Electrochemical Systems, third ed., Wiley-Interscience, 2004.

[22] P. Arora, M. Doyle, A.S. Gozdz, R.E. White, J. Newman, J. Power Sources 88 (2000) 219—231.

[23] X. Zhang, W. Shyy, A.M. Sastry, J. Electrochem. Soc. 154 (2007) 910—916.

[24] Y.T. Cheng, M.W. Verbrugge, J. Appl. Phys. 104 (2008) 083521.

[25] A. Bower, P. Guduru, V. Sethuraman, J. Mech. Phys. Solids 59 (2011) 804—828.

[26] K. Zhao, M. Pharr, S. Cai, J.J. Vlassak, Z. Suo, J. Am. Ceram. Soc. 94 (2011) S226—S235.

[27] Z. Cui, F. Gao, J. Qu, J. Mech. Phys. Solids 60 (2012) 1280—1295.

[28] T. Mori, K. Tanaka, Acta Metall. 21 (1973) 571—574.

[29] Y. Benveniste, Mech. Mater. 6 (1987) 147—157.

[30] Y. Benveniste, G. Dvorak, in: Micromechancis and Inhomogeneity, Springer, New York, 1990.

[31] S. Golmon, K. Maute, S.-H. Lee, M.L. Dunn, Appl. Phys. Lett. 97 (2010).

[32] N. Olhoff, Struct. Multidis. Optim. 1 (1989) 11—17, http://dx.doi.org/10.1007/BF01743805.

[33] K. Svanberg, SIAM J. Optim. 12 (2002) 555—573.

[34] P.V. den Bossche, F. Vergels, J.V. Mierlo, J. Matheys, W.V. Autenboer, J. Power Sources 162 (2006) 913—919.